Journal Name

Preprint:
The published version is available from Plasma Sources Science and Technology:
https://doi.org/10.1088/1361-6595/aeb828

Crossmark

RECEIVED
dd Month yyyy

REVISED
dd Month yyyy

PAPER

Influence of Surface Charging on the Electrohydrodynamic Effect in Linear Plasma Synthetic Jet Actuator

Yuki ISHII[1], Atsushi KOMURO[2], Shūji ŌTOMO[1,3] and Hiroyuki NISHIDA[1,*]

[1]Department of Mechanical Systems Engineering, Tokyo University of Agriculture and Technology, 2-24-16, Naka-cho, Koganei, 184-8588, Tokyo, Japan

[2]Environmental Management Research Institute, National Institute of Advanced Industrial Science and Technology (AIST), 16-1 Onogawa, Tsukuba, Ibaraki, 305-8569, Japan

[3]Laboratory for Flow Control (LFC), School of Engineering, Hokkaido University, N13W8, Sapporo, 060-8628, Hokkaido, Japan

*Author to whom any correspondence should be addressed.

E-mail: hnishida@cc.tuat.ac.jp

Keywords: Electrohydrodynamics, Fluid dynamics, Pockels effect

Abstract

Dielectric Barrier Discharge Plasma Actuator (DBD-PA) generates Electrohydrodynamic (EHD) force via the interaction between an electric field and charged particles. Linear Plasma Synthetic Jet Actuator (LPSJA) utilizes opposing DBD-PA to induce a vertical jet through the collision of induced flows; however, the effect of the electrode distance (λ) on its performance remains unclear. Clarifying this relationship requires investigating the electric field distribution because it directly drives the EHD force. In this study, we evaluated the electrical and fluid dynamic characteristics of the LPSJA using Pockels measurement and Particle Image Velocimetry (PIV). Our results demonstrate that reducing λ intensifies the local electric field due to the accumulation of surface charges in preceding discharge phase, which promotes initial EHD force generation. Nevertheless, this localized enhancement does not directly correlate with the global flow velocity. At small λ, the output is significantly restricted by complex fluid dynamic effects, particularly the increased pressure gradient from colliding ionic winds. We characterize the LPSJA performance as a result of the competition between electrical EHD force promotion and fluid dynamic losses. This study provides a practical basis for optimizing Plasma Synthetic Jet Actuator configurations, facilitating more effective design strategies that account for the complex interaction between electrical and fluid dynamic factors.

1 Introduction

Dielectric Barrier Discharge Plasma Actuator (DBD-PA) is an active flow control device using Electrohydrodynamic(EHD) effect [1, 2]. As shown in Fig. 1 (a), DBD-PA typically consists of two electrodes separated by a dielectric. When high AC voltage is applied between the electrodes, DBD-PA produces surface discharge and plasma. Then, charged particles within the plasma are accelerated by electric field between the electrodes. These charged particles collide with neutral air particles, creating an EHD force and a surface flow known as ionic wind. Because of this driving mechanism, DBD-PA offers several advantages, including a structure with no mechanical moving parts, lightweight and thin design, and high active controllability. Due to these advantages, DBD-PA has attracted significant attention for applications such as controlling airflow separation [3, 4, 5], turbulent friction drag [6, 7, 8], bluff-body flow [9, 10, 11] and heat transfer [12, 13, 14, 15].

The Plasma Synthetic Jet Actuator (PSJA), a derivative of DBD-PA, has been also widely studied due to its higher flow controllability [16, 17, 18, 19]. In the PSJA, the AC electrodes are positioned to face each other in cross-section to produce an upward-directed ionic wind (Fig. 1 (b)). This configuration allows PSJA to control flow over a wider area and with greater flexibility. PSJA are generally classified into the Linear-type PSJA (LPSJA, Fig. 1 (c)) and the Annular-type PSJA (APSJA, Fig. 1 (d)). LPSJA features linear upper electrodes in an array, while APSJA utilizes circular upper electrodes. The performance of these actuators is highly dependent on the electrode

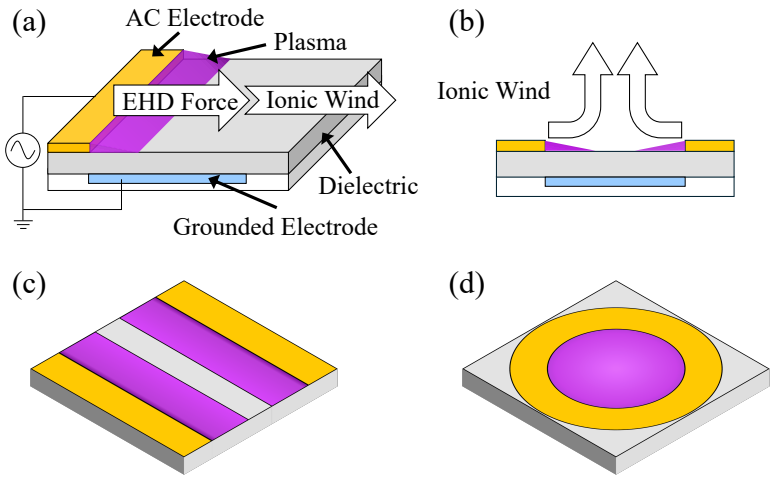


Figure 1. Plasma actuator configurations. (a) Conventional DBD-PA (Single PA). (b) Cross-sectional view of a Plasma Synthetic Jet Actuator (PSJA). (c) Linear-type PSJA (LPSJA) and (d) Annular-type PSJA (APSJA).

arrangement, which determines the spatial distribution of the EHD force and the resulting flow structure. While conventional DBD-PA primarily produces momentum parallel to the wall, the facing electrode configurations of PSJA enable the generation of a concentrated vertical jet. It has been demonstrated that this colliding jet configuration offers superior flow control effectiveness compared to standard arrangements, as it provides greater momentum penetration into the external flow [20]. In particular, LPSJA have been used as plasma vortex generators; by inducing spanwise wall jets that interact with the oncoming boundary layer, they create strong streamwise vortices to suppress flow separation on airfoils [20] and vehicles [21, 22]. In contrast, APSJA concentrates the EHD force toward a central focal point, producing a localized, high-intensity synthetic jet. This specific flow characteristic is expected to be advantageous for the active control of turbulent friction drag, as it allows for direct, three-dimensional interaction with the near-wall coherent structures.

However, the relationship between AC electrode arrangement and ionic wind characteristics has not yet been clarified. Wicks et al. [23] experimentally showed that an optimal AC electrode distance (λ) exists to maximize the vorticity of the flow induced by LPSJA. Saito et al. [24] demonstrated that changing λ can either weaken or strengthen the discharge propagation length and light emission intensity compared to conventional DBD-PA (Single PA). Regarding APSJA, Humble et al. [25] and Fridlender et al. [26] reported that the flow direction reverses when electrode inner diameter λ is small. Borradaile et al. [27] numerically investigated the cause of this flow reversal and proposed that decreasing λ increases the curvature of the electric field lines, leading to a higher concentration of the electric field near the electrode edges. This intensified field promotes the rapid accumulation of surface charges on the dielectric, which quickly elevates the surface potential and thereby reduces the effective potential difference between the AC electrode and the dielectric surface. Consequently, the reduced potential difference suppresses the discharge propagation, limiting the spatial and temporal extent of the EHD force generation.

Indeed, such influence of surface charge accumulation on the discharge process is a fundamental characteristic of DBD-PA [28, 29]. Since these actuators are driven by AC high voltage, the discharge is inherently unsteady and governed by the "memory effect" of the accumulated charges [30]. As illustrated in Fig. 2, the discharge evolves through distinct phases: a filamentary streamer during the positive-going phase and a diffusive glow during the negative-going phase [1]. Charges accumulated in one phase significantly affect the local electric field in the subsequent phase, thereby modulating the discharge intensity and the resulting plasma motion [31]. Therefore, to fully understand the ionic wind behavior, it is essential to resolve the temporal evolution of the surface charging and its direct impact on EHD force generation.

In the case of PSJA, the proximity of opposing electrodes is hypothesized to induce even more complex variations in surface potential compared to these Single PA mechanisms. The overlapping discharge regions may lead to unique potential repulsion or enhancing effects (Fig. 2), which significantly alter the magnitude and spatial distribution of the EHD force, thereby modifying the resulting ionic wind behavior. To resolve these unsteady phenomenon, it is essential to perform time-resolved measurements that can capture the temporal evolution of both the surface potential and the resulting flow field. However, such a perspective has not yet been applied to investigate the

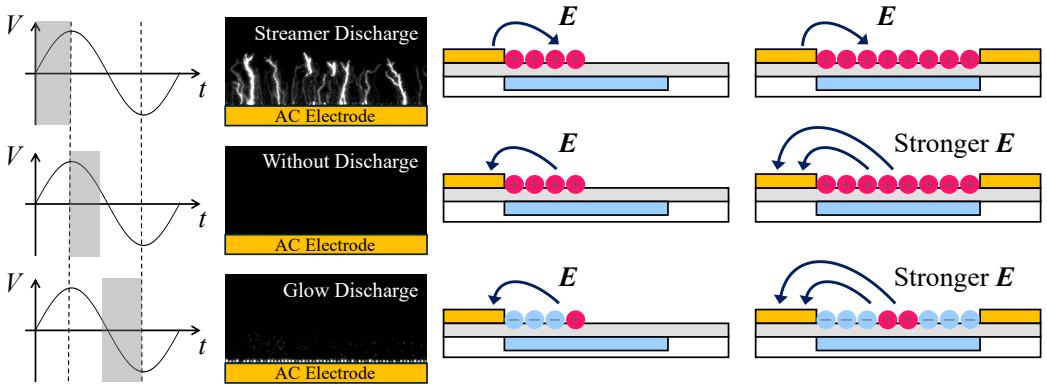


Figure 2. Mechanism of output variation in LPSJA. The left figure shows the progression of the voltage phase. The center figure displays the discharge emission photograph. The right figure illustrates the electric field enhancement mechanism due to surface charging. This figure represents how the increased accumulation of positive surface charges in the PSJA configuration enhances the local electric field.

electrode interference in the PSJA. Consequently, direct experimental evidence verifying how dynamic surface charging modulates the EHD force in PSJA geometry has not yet been established.

To this end, the objective of this study is to clarify how the dynamic surface charging modulates both the local electric field and the resulting EHD force generation in the LPSJA. The LPSJA is selected as the primary target of this investigation because its two-dimensional configuration provides a more fundamental and simplified system compared to the complex, three-dimensional flow field of the APSJA. To achieve this, first, we compare the phase-resolved surface potential distribution and the velocity field of the LPSJA with those of a conventional Single PA. In this analysis, $\lambda = 8$ mm is selected as a representative case to provide a clear baseline for identifying the fundamental interactions unique to the LPSJA. Next, we evaluate the effect of varying λ to understand how these physical interactions scale with the electrode configuration. Finally, we discuss the overall actuator performance, such as time-averaged power consumption and momentum flow rate, to clarify how the localized discharge dynamics govern the total device efficiency.

2 Experimental Methods

2.1 Experimental setup and conditions

Figure 3(a) shows the configuration of LPSJA. We used a copper tape (Teraoka, 8323) for the AC electrode. The thickness of the electrodes was 35 µm, the width was 5 mm, and spanwise direction was 20 mm. Its discharge-side edge is serrated shape with 1 mm height and 1 mm wide as in Fig. 3(b). The serrated geometry was employed to promote local electric field concentration at the tips, thereby stabilizing the discharge and fixing the discharge positions. In this study, the distance between the serrated tips of the two opposed electrodes is defined as λ. To investigate the influence of electrode proximity, λ was varied across a range from 4 mm to 20 mm. The specific values of λ used for each measurement case are detailed in the subsequent sections of this paper. The dielectric is a 50 mm square, 1 mm thick $Bi_4Ge_3O_{12}$ (BGO) crystal. This material was selected as an electro-optic sensor that exhibits the Pockels effect, a linear electro-optic phenomenon where the refractive index of the crystal changes in proportion to the applied electric field [32]. This effect induces optical birefringence, which causes a phase shift in the light transmitted through the crystal [33]. To provide this optical measurement, a 40 mm square transparent indium tin oxide (ITO) was employed as the grounded electrode. The combination of the BGO crystal and the transparent ITO electrode provides the necessary optical access for non-intrusive surface potential imaging. The AC electrodes and the grounded electrode overlap completely. For all measurements, we powered LPSJA with a 5 kHz sine wave with an amplitude of 6 to 10 kV_{pp}.

2.2 Velocity field measurement

We performed both time-averaged and voltage-phase-locked two-dimensional Particle Image Velocimetry (PIV) to characterize the flow field induced by the ionic wind. Figure 5 (a) shows the PIV measurement apparatus, which consists of a sCMOS camera (Andor, Neo 5.5, 2560 × 2160 pixels) and a double-pulse Nd-YAG laser (Litron Lasers, Nano S 30-15 PIV). The laser provided pulses with a wavelength of 532 nm, a maximum energy of 30 mJ/pulse, and a duration of 5-8 ns. The laser and camera were synchronized by a Timing Controller (LabSmith, LC880) at a sampling

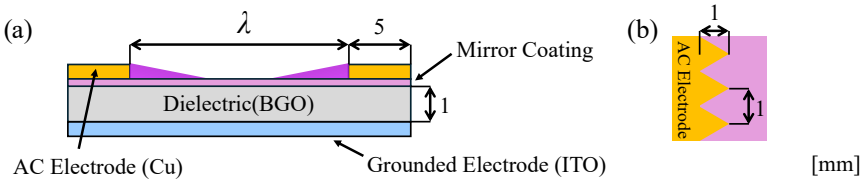


Figure 3. Detailed configuration of the LPSJA setup. (a) Side view showing the layered structure of the AC electrodes, the 1 mm thick BGO dielectric crystal, and the transparent ITO grounded electrode. (b) Top view showing the serrated electrode geometry of AC electrodes.

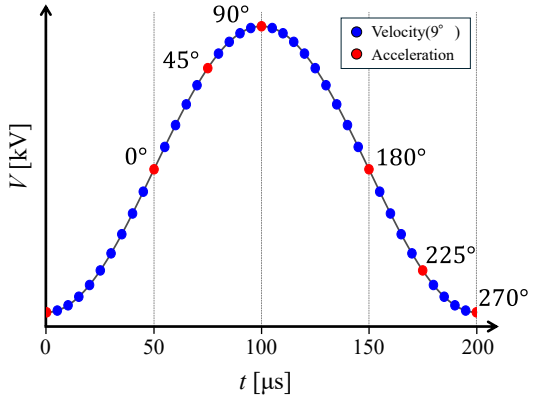


Figure 4. Timing of the phase-locked PIV measurements relative to the applied voltage waveform. Measurements were performed at 9° intervals (5 µs), dividing one voltage cycle into 40 phases. From these measured velocity fields, the local acceleration fields were derived at key phases ($0°, 45°, 90°, 180°, 225°$, and $270°$)

frequency of 10 Hz. We placed the LPSJA inside a stainless steel chamber filled with incense smoke (solid particles smaller than 1 µm). The Stokes number of the tracer particles was estimated to be 5.5×10^{-4}, confirming that the particles sufficiently follow the flow. The camera was equipped with a single-focal-length lens (Nikon, AI AF Micro-Nikkor 200 mm $f/4$D IF-ED) and a band-pass filter to remove plasma emission from the images. The imaging area resolution was approximately 0.005 mm/pixel. The velocity vectors were calculated using a multi-grid correlation algorithm provided by the software (SEIKA Digital Image Co., Koncerto II). The interrogation window size was iteratively decreased from 96×96 pixels to a final size of 32×32 pixels with a 75% overlap. The time interval between pulses was adjusted to 10 µs to yield a maximum characteristic particle displacement of approximately 8 pixels. This setting resulted in a vector grid spacing of 8 pixels (0.04 mm), while the effective physical resolution corresponds to the window size of 0.16 mm. Both the time-averaged and phase-averaged velocity fields were obtained by ensemble averaging at least 250 pairs of images for each measurement condition. Moreover, as a post-processing step, a median filter was applied to remove spurious vectors. In this process, any vector whose absolute deviation from the median of its 3×3 neighboring grid exceeded 30.0 was removed (approximately 2% of total vectors).

The phase-locked PIV was performed by adjusting the signal delay of a function generator synchronized with the laser and the camera. For each phase, the voltage-phase-averaged velocity field was obtained by ensemble-averaging 250 instantaneous image pairs to capture the periodic evolution of the flow. As shown in Fig. 4, measurements were taken at intervals of 9° (5 µs), corresponding to the voltage cycle divided into 40 equal increments.

In this study, to analyze the characteristics of the EHD force based on the time variation of flow field, we utilized the incompressible Navier-Stokes equations:

$$\rho \frac{D\mathbf{u}}{Dt} = \rho \left(\frac{\partial \mathbf{u}}{\partial t} + (\mathbf{u} \cdot \nabla)\mathbf{u} \right) = -\nabla p + \mu \nabla^2 \mathbf{u} + \mathbf{F}_{EHD} \tag{1}$$

where $\mathbf{F}_{EHD}$ is the EHD force. Especially during the transient phases of the discharge where the electric field fluctuates rapidly, the acceleration term $D\mathbf{u}/Dt$ dominates the momentum balance. Our order-of-magnitude analysis confirms that the viscous term is negligible relative to the

advection term. Consequently, the EHD force is primarily balanced by the acceleration term and the pressure gradient:

$$\mathbf{F}_{EHD} \approx \rho \frac{D\mathbf{u}}{Dt} + \nabla p \tag{2}$$

The measured acceleration term $\mathbf{a} = D\mathbf{u}/Dt$ is a key indicator that reflects the impact of the EHD force, while inherently including the contribution of the induced pressure field. This relationship implies that the observed acceleration is a direct manifestation of the instantaneous EHD force ($\mathbf{F}_{EHD}$) and the induced pressure gradient. The acceleration term $\mathbf{a}$ was calculated by summing the local acceleration and the advection term, both derived from the phase-averaged velocity fields. The local acceleration $\partial\mathbf{u}/\partial t$ was calculated using a central difference scheme [34]:

$$\frac{\partial \mathbf{u}}{\partial t}(\theta) = \frac{\mathbf{u}(\theta + \Delta\theta) - \mathbf{u}(\theta - \Delta\theta)}{2\Delta t} \tag{3}$$

where $\Delta\theta = 18°$ (corresponding to $2\Delta t = 20$ µs) was selected as the time interval. The advection term $(\mathbf{u} \cdot \nabla)\mathbf{u}$ was computed by applying a second-order central difference to the spatial velocity gradients, consistent with the grid resolution of the PIV analysis ($\Delta x, \Delta y \approx 0.03$ mm). This interval was chosen based on a sensitivity analysis to balance the trade-off between temporal resolution and the signal-to-noise ratio. While a smaller $\Delta\theta$ (9°) could capture higher-frequency fluctuations, it significantly amplified the PIV measurement uncertainty. The selected $\Delta\theta$ of 18° effectively filtered out high-frequency noise while remaining sufficient to capture the primary EHD-driven transient behavior. The measurement uncertainty in the acceleration term, δa, was evaluated by considering the error propagation from both the temporal and spatial derivatives. First, the uncertainty in the local acceleration $\partial\mathbf{u}/\partial t$ was derived using the standard error propagation method applied to Eq. (3). Given the phase-averaged velocity uncertainty of approximately 0.003 m/s (based on 250 image pairs), the uncertainty in acceleration was estimated to be approximately 210 m/s^2. Subsequently, the additional uncertainty arising from the advection term $(\mathbf{u} \cdot \nabla)\mathbf{u}$ was incorporated. Based on the spatial resolution ($\Delta x, \Delta y \approx 0.03$ mm) and the maximum induced velocity (approximately 4 m/s), the uncertainty in the advection term was determined to be approximately 400 m/s^2. By combining these components, the total uncertainty in the acceleration term δa was estimated to be approximately 450 m/s^2. This value is negligible compared to the maximum observed acceleration (on the order of 10^4 m/s^2), confirming that the measurement precision is sufficient to discuss the transient EHD dynamics.

2.3 Surface potential distribution measurement

We employed the Pockels measurement [33] for the surface potential distribution. Figure 5 (b) shows the measurement system, which consists of an LED, a Polarized Beam Splitter (PBS), an eighth-wave plate, and a high-speed camera (Photron, FASTCAM Mini AX). The light from an LED, powered by a Regulated DC power supply (TEXIO, PSW-360L30), is linearly polarized by the PBS. The light then passes through an eighth-wave plate, introducing a phase difference of $\pi/4$ between the two orthogonal vibration components. Subsequently, the light passes through the Pockels crystal (LPSJA dielectric) and reflects off the mirror surface. Passing through an eighth-wave plate again introduces an additional $\pi/4$ phase difference. In the absence of a surface potential difference, the reflected light is circularly polarized. However, when an electric field is applied, the light becomes elliptically polarized due to a phase difference proportional to the electric field strength. Finally, when the PBS re-linearly polarizes and reflects the light, the phase difference manifests as light intensity. The high-speed camera captured these intensity variations at a frame rate of 10,000 fps with a shutter speed of 1/100, 000 s. The image resolution was set to 768×256 pixels, providing a spatial resolution of approximately 0.02 mm/pixel. Prior to the discharge experiments, the Pockels measurement system was calibrated following the procedure of Natsume et al. [35]. DC voltages of known magnitude were applied to the electrodes, and the light intensity distributions were recorded with the high-speed camera. From these data, a calibration curve relating light intensity to surface potential was obtained and confirmed to be linear over the voltage range investigated in this study. Using this calibration curve, each recorded image was converted to a surface potential distribution. For consistency with the velocity field analysis, the surface potential was evaluated at the same phases as the acceleration derivation ($0°, 45°, 90°, 180°, 225°$, and $270°$). We conducted the measurement over 99 cycles immediately following the voltage application.

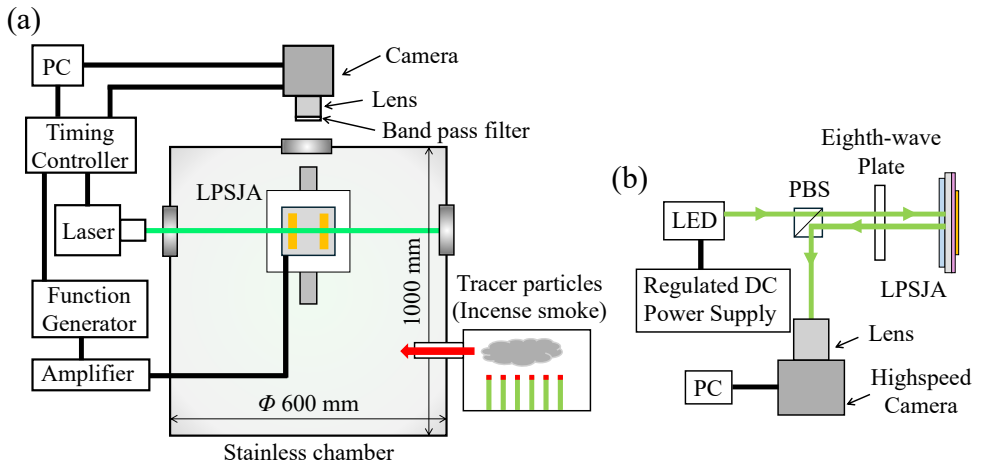


Figure 5. Schematic illustration of the experimental apparatus: (a) particle image velocimetry (PIV), and (b) pockels measurement.

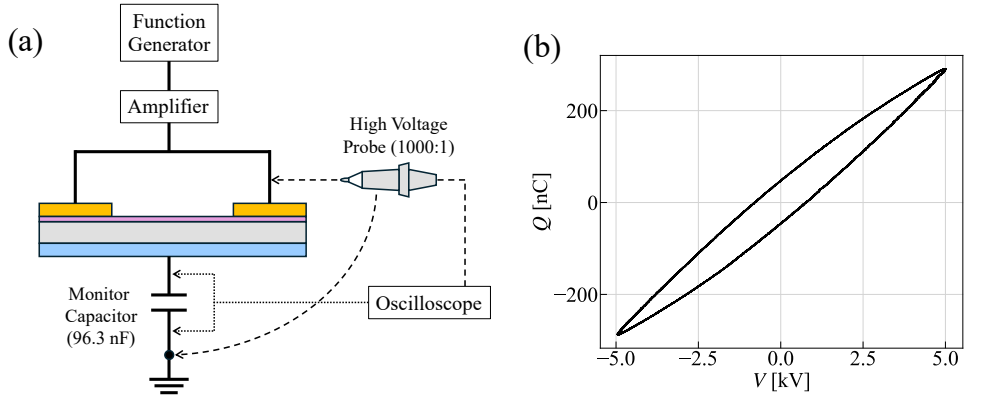


Figure 6. Setup for Power consumption measurement. (a) Circuit diagram for the V-Q Lissajous method, featuring a monitoring capacitor to capture the instantaneous charge Q. (b) A typical V-Q Lissajous curve. The area enclosed by the Lissajous loop represents the energy dissipation per cycle, from which the average power consumption P_{elec} is derived. To ensure data reliability, measurements are averaged over 100 AC cycles and repeated three times for each case.

2.4 Power consumption measurement

We performed power consumption measurements using the V-Q Lissajous method to investigate the electrical characteristics of LPSJA. Figure 6 shows the measurement system and the V-Q Lissajous curve. A function generator generated the voltage waveform, which was then amplified and applied to LPSJA. We inserted a monitoring capacitor into the circuit. We obtained the instantaneous charge Q from the voltage across the monitoring capacitor and its capacitance. For noise reduction, the voltage of the monitoring capacitor is averaged over 100 AC cycles. By plotting Q against the instantaneous applied voltage V, we obtained the V-Q Lissajous curve. Calculating the area inside the curve yields the power consumption. We performed the measurement at least three times for one experimental case and averaged all three results.

3 Experimental Results

3.1 Comparison of LPSJA and Single PA

3.1.1 Temporal evolution of velocity field

In this section, we investigate the impact of the opposing electrode by comparing the LPSJA with Single PA. The case of $\lambda = 8$ mm is selected as a representative baseline to clarify the fundamental differences in their discharge and induced flow behaviors. We first focus on the temporal evolution of the velocity field to identify the key mechanisms underlying the jet formation process. Figures 7(a) and (b) illustrate an example of velocity fields and the locations of u_{max} for the Single PA and the LPSJA ($\lambda = 8$ mm), respectively. In the Single PA (Fig. 7(a)), the induced

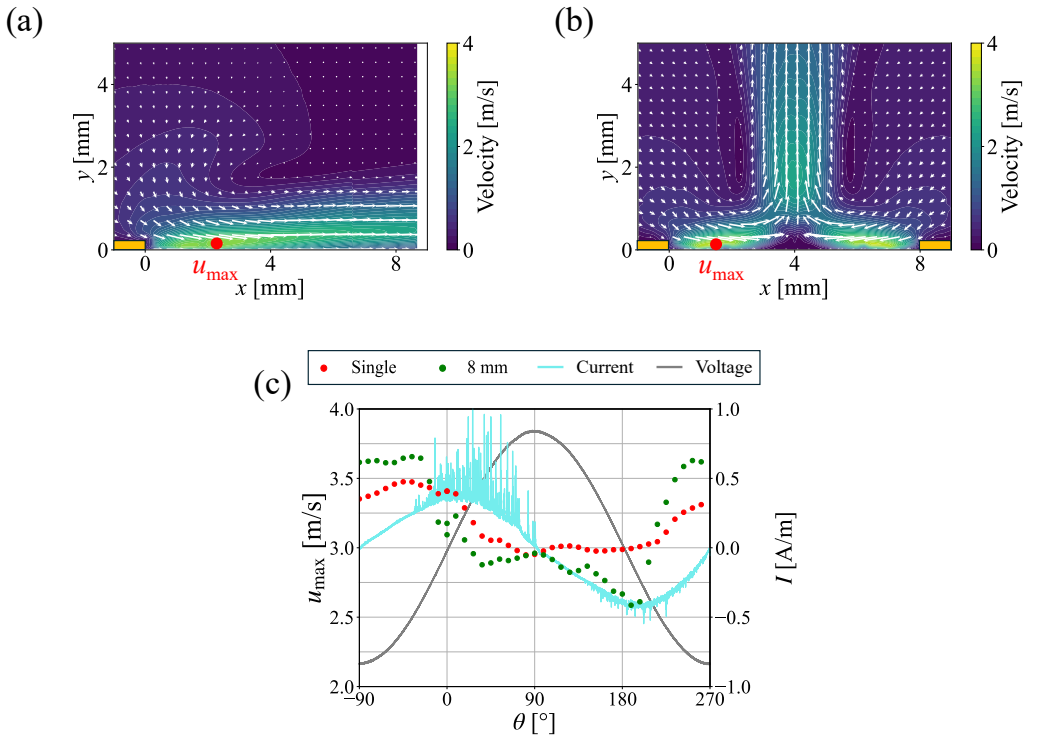


Figure 7. Comparison of induced flow dynamics between (a) Single PA and (b) LPSJA ($\lambda = 8$ mm). Velocity fields showing the horizontal wall jet in the Single PA versus the colliding and vertically deflected jet in the LPSJA. The markers indicate the spatial locations of the maximum horizontal velocity u_{max}. (c) Temporal evolution of u_{max} relative to the applied voltage (gray) and current waveforms (light blue). Notably, the LPSJA exhibits an earlier onset of both acceleration and deceleration compared to the Single PA, with significantly larger velocity fluctuations.

ionic wind propagates horizontally along the dielectric surface, forming a typical wall-jet structure that extends downstream. In contrast, for the LPSJA (Fig. 7(b)), the ionic winds generated from the two opposing electrodes propagate toward each other, collide at the center, and are subsequently deflected in the vertical y-direction. Despite these structural differences, the u_{max} is located near the electrodes and its temporal evolution is presented in Fig. 7(c). The vertical and horizontal axes represent the magnitude of u_{max} and the voltage phase, respectively. In this figure, the applied voltage V and current waveforms I are indicated by gray and light blue solid lines. Regarding the velocity trends, both the $\lambda = 8$ mm and the Single PA exhibit deceleration during the positive-going voltage phase and acceleration during the negative-going phase. This result is consistent with previous studies reporting that EHD force generation is primarily governed by negative-going phase [1]. However, a closer comparison reveals distinct differences in the dynamics of these phases. In the $\lambda = 8$ mm, both the initiation of deceleration (during the positive-going phase) and the onset of acceleration (during the negative-going phase) occur at an earlier phase compared to the Single PA. Furthermore, the magnitude of these velocity changes is significantly larger in the LPSJA configuration, indicating that the working fluid undergoes more rapid acceleration and deceleration. Based on the Navier-Stokes equations, these velocity dynamics correspond to the local acceleration term $\partial u/\partial t$. The sharp increase and decrease in velocity at specific phases reflect the instantaneous impact of the resulting force acting on the fluid at those moments. The enhanced and rapid deceleration in the LPSJA is primarily attributed to fluid dynamic interactions; specifically, the collision of opposing ionic winds creates a high-pressure region that induces a strong adverse pressure gradient. In contrast, the enhanced and rapid acceleration observed during the negative-going phase is a direct consequence of the intensified EHD force. The earlier onset and higher peak of the local acceleration in the LPSJA suggest that the symmetrical electrode arrangement not only strengthens the EHD force but also significantly improves its responsiveness to the voltage waveform. This enhanced and more rapid force generation is likely coupled with the modified surface potential distribution, which we investigate in the following section to clarify the underlying electrical-to-mechanical energy conversion mechanism.

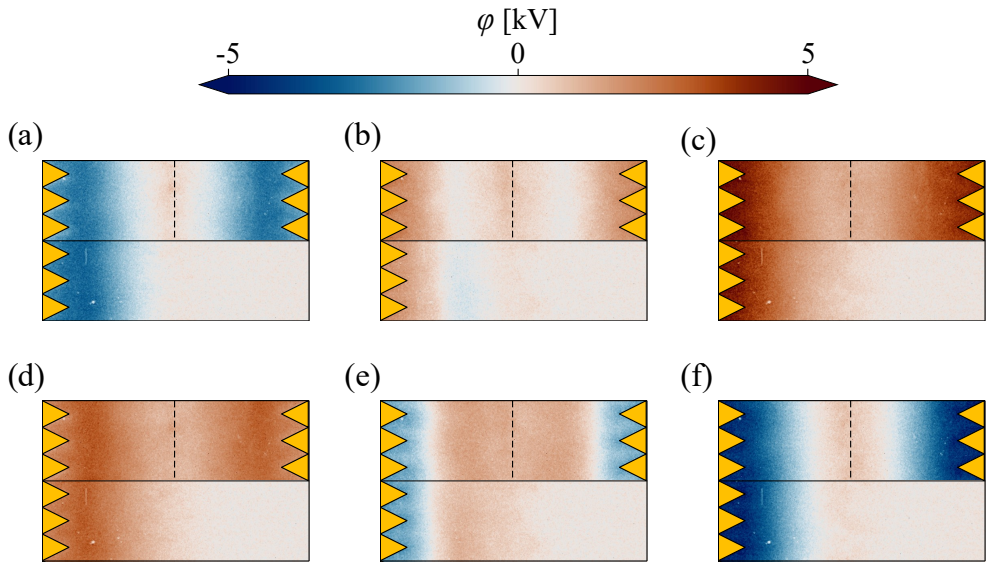


Figure 8. Spatio-temporal evolution of surface potential ϕ. Figure (a)–(c) and Fig. (d)–(f) show the positive-going phase ($0°, 45°$, and $90°$) and negative-going phases ($180°, 225°$, and $270°$), respectively. In each figure, the top half corresponds to the LPSJA, while the bottom half shows the Single PA. Note the clear asymmetry in charge propagation: in the positive phase (c), the discharges from opposing electrodes approach at the center ($x = 4$ mm), whereas in the negative phase (f), the negative potential does not reach the center.

3.1.2 Temporal evolution of surface potential distribution

Figure 8 presents the phase-averaged potential ϕ distributions from the 66th to the 99th cycle, shown from a top-view perspective. Figure 8(a)–(c) corresponds to the positive-going phase ($0°, 45°$, and $90°$), and Fig. 8(d)–(f) represents the negative-going phase ($180°, 225°$, and $270°$). In each figure, the top and bottom half shows the results for the LPSJA and Single PA, respectively. The orange regions of each figure indicate the positions of the opposing serrated electrodes. The red and blue regions represent positive and negative surface potentials, respectively.

In the positive-going phase, at $0°$(Fig. 8(a)), a residual negative potential from the preceding negative-going phase is observed. As the phase progresses through $45°$ to $90°$(Fig. 8(b),(c)), the positive potential region (indicated in red) expands toward the center of the dielectric surface. Notably, at $90°$ (Fig. 8(c)), the discharge regions from the opposing electrodes approach in the LPSJA, resulting in a stronger positive charge accumulation across the center of the electrode distance ($x = 4$ mm).

Conversely, Fig. 8 (d)–(f) representing the negative-going phase, a residual positive potential from the preceding positive-going phase remains at $180°$(Fig. 8(d)). While negative charges (indicated in blue) accumulate and gradually neutralize the residual potential by $270°$ (Fig. 8(f)), the spatial distribution is different from the positive phase. Even at $270°$ (Fig. 8(f)), the negative potential remains localized near the electrode edges and does not reach the center. In contrast to the Single PA, a higher positive residual potential persists in the central region ($x = 4$ mm) of the LPSJA, maintaining the charged state established during the preceding positive phase. This spatial difference in the charging area is attributed to the differences in propagation lengths of the two discharge modes. Specifically, the streamer-like discharge reaches the center due to its longer propagation length, whereas the glow-like discharge has a shorter propagation length and fails to neutralize the existing positive potential.

To quantitatively evaluate the results, Fig. 10 shows the x-direction profiles of the surface potential distribution. The x-range is plotted from the electrode edge ($x = 0$ mm) to the midpoint of the electrode distance ($x = 4$ mm). The x-directional profiles were extracted from the surface potential distribution measurements by averaging over three adjacent pixels (Fig. 9). This process was repeated for three cross-sections at the electrode edge, and their spatial average was calculated. The dashed line represents this averaged profile, with the error envelopes indicating the 95% confidence area evaluated from the 66th to 99th voltage cycles. To evaluate the underlying trends, a two-dimensional Savitzky-Golay (SG) filter was first applied to the entire potential distribution for spatial noise reduction. Subsequently, the x-directional profiles (solid lines) were extracted from the filtered distribution by averaging the values across the three representative cross-sections mentioned above. This filtering process effectively suppresses measurement noise while accurately

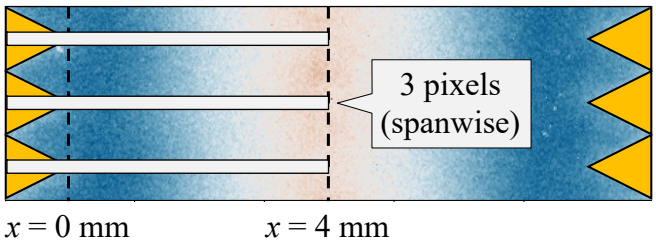


Figure 9. Procedure for x-directional potential profile extraction. The diagram illustrates the spatial averaging process across three representative cross-sections at the electrode edge. This method, combined with a two-dimensional Savitzky-Golay filter, ensures effective noise reduction while preserving the essential spatial characteristic of surface potential distribution.

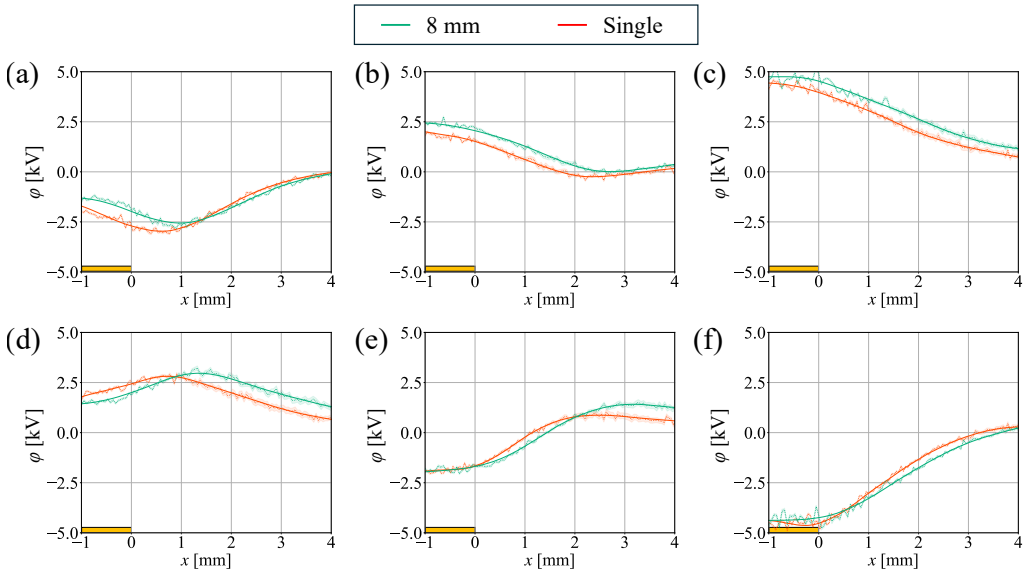


Figure 10. Comparison of x-directional surface potential profiles between Single PA and LPSJA ($\lambda = 8$ mm). Figure (a)–(c) and (d)–(f) show the positive-going phase ($0°, 45°$, and $90°$) and negative-going phases ($180°, 225°$, and $270°$), respectively. The dashed line represent the raw spatially averaged profiles, with error envelopes indicating the 95% confidence area evaluated across the 66th to 99th voltage cycles. The solid lines indicate the filtered profiles. Notably, the LPSJA maintains a higher positive potential during the positive phase (c) and the onset of the negative phase (d), indicating enhanced charge accumulation due to the interacting discharge regions.

preserving the essential spatial gradients and underlying trends of the original profiles.

Regarding the comparative performance of the two configurations, both the Single PA and the LPSJA ($\lambda = 8$ mm) exhibit a similar cyclic charging process, yet with differences in magnitude. In the positive-going phase ($0°$ to $90°$, Fig. 10(a)–(c)), both cases initially show a negative residual potential at $0°$ due to the preceding negative-going phase. As the phase progresses, these residual charges are neutralized, and positive charges accumulate. Notably, the LPSJA exhibits a significantly higher surface potential than the Single PA throughout this phase. This elevated potential level indicates a more positive charge accumulation, which is facilitated by the approaching discharges from the opposing electrodes.

A similar trend is observed in the negative-going phase ($180°$ to $270°$, Fig. 10(d)–(f)). At the onset ($180°$, Fig. 10(d)), the dielectric surface in both cases remains positively charged as a result of the preceding positive-going phase. However, the LPSJA starts with a higher residual potential than the Single PA. As the phase progresses toward $270°$ (Fig. 8(f)), negative charging becomes evident within the glow-like discharge region. Interestingly, in the case of the LPSJA ($\lambda = 8$ mm), the potential profiles for both configurations eventually converge at $270°$, as the negative discharge effectively neutralizes the surface. This suggests that while the LPSJA significantly enhances charge accumulation during the positive phase, the subsequent negative discharge makes the potential state go back to the level comparable to that of the Single PA by the end of the cycle.

3.1.3 Influence of surface potential distribution on flow field

The influence of surface charging on EHD force generation and the resulting flow dynamics is evaluated by investigating the spatiotemporal correlation between the surface potential and the acceleration term of flow. The electric field profiles were derived by calculating the x-direction gradient of the potential distribution shown in Fig. 10. In dielectric barrier discharges, the EHD force originates from the momentum transfer between ions and neutral molecules [3]. Specifically, during the positive-going phase, the acceleration of positive ions by a positive electric field generates a positive EHD force. Conversely, during the negative-going phase, the acceleration of negative ions by a negative electric field similarly produces a positive EHD force[36]. Consequently, the EHD force that drives the flow in the positive direction is intensified by the enhancement of the positive electric field during the positive-going phase, and by the enhancement of the negative electric field during the negative-going phase.

Based on this criterion, Fig. 11 compares the phase-averaged x-directional acceleration term (Du/Dt, a) distributions with the surface electric field E profiles during the positive-going phase. In this figure, the top and middle panel represent the acceleration term for the LPSJA ($\lambda = 8$ mm) and the Single PA, respectively while the bottom panel shows the corresponding electric field profiles. In the acceleration term maps, the red-colored regions indicate positive acceleration (flow acceleration), while the blue-colored regions indicate negative acceleration (flow deceleration). The analysis focuses on three representative phases: (a) 0°, (b) 45°, and (c) 90°.

First, focusing on the electrical characteristics, the spatiotemporal evolution of the surface electric field is examined. The derived electric field profiles indicate that the magnitude of E for the LPSJA is consistently enhanced compared to the Single PA. Notably, the position of this enhancement moves further downstream as the phase progresses, corresponding to the propagation of the discharge along the dielectric surface. While the electric field near the electrode edge reaches a plateau once the surface becomes fully charged, the active discharge front travels toward the center ($x = 4$ mm). This results in a continuous downstream shift of the peak electric field enhancement.

This enhancement is attributed to the increased surface charge density in the LPSJA due to the proximity of the opposing electrodes, which subsequently strengthens the memory effect. From the perspective of potential and electric field distributions, it is predicted that the EHD force generation would be promoted for $\lambda = 8$ mm, particularly at the beginning of the phase where the electrical advantage is most pronounced.

To verify this prediction, the resulting flow response is analyzed by focusing on the spatiotemporal evolution of the acceleration term fields. However, the observed acceleration term reveals a more complex behavior than what is predicted only by the electric field intensity.

In the 0° (Fig. 11(a)), both cases exhibit significant negative acceleration, as indicated by the broad blue-colored regions. As noted in the previous discussion, this deceleration is most prominent in the downstream region($x > 1$ mm) where the electric field still maintains negative values. Nevertheless, a clear difference is observed near the electrode edge ($x < 1$ mm). In the LPSJA, the enhanced electric field shifts to positive values more rapidly, resulting in a smaller magnitude of negative acceleration compared to the Single PA. Furthermore, a positive acceleration region (red) is observed in the immediate vicinity of the electrode, suggesting that the flow has already begun to transition toward acceleration in this near-field area. This indicates that the electrical enhancement effectively suppresses flow deceleration at this early stage.

As the phase progresses to 45° (Fig. 11(b)), the positive electric field region expands downstream, and a corresponding positive acceleration region emerges and spreads. While the electric field for the LPSJA remains stronger and continues to shift its peak downstream, the acceleration for the LPSJA is unexpectedly smaller than that of the Single PA in this phase. This discrepancy suggests that while the enhanced electric field promotes EHD force generation, its contribution is counteracted by fluid dynamic losses. In the LPSJA,the propagation of the discharge toward the center ($x = 4$ mm) leads to the collision of ionic winds originating from the opposing electrodes. This interference creates a high-pressure region near the stagnation point, inducing a strong adverse pressure gradient against the x-direction flow. Therefore, the lower acceleration observed in 45° (Fig. 11(b)) is attributed to the fact that the decelerating effect of the adverse pressure gradient partially overcomes the increase in EHD force.

Figure 12 shows the spatiotemporal evolution of the acceleration and electric field during the negative-going phase. Similar to the positive-going phase, the behavior of the surface electric field is first examined. Throughout this period, the electric field for the LPSJA is consistently enhanced in the negative direction compared to the Single PA. Notably, the peak of this negative electric field enhancement shifts downstream as the phase progresses from 180° (Fig. 12(d)) to 225°

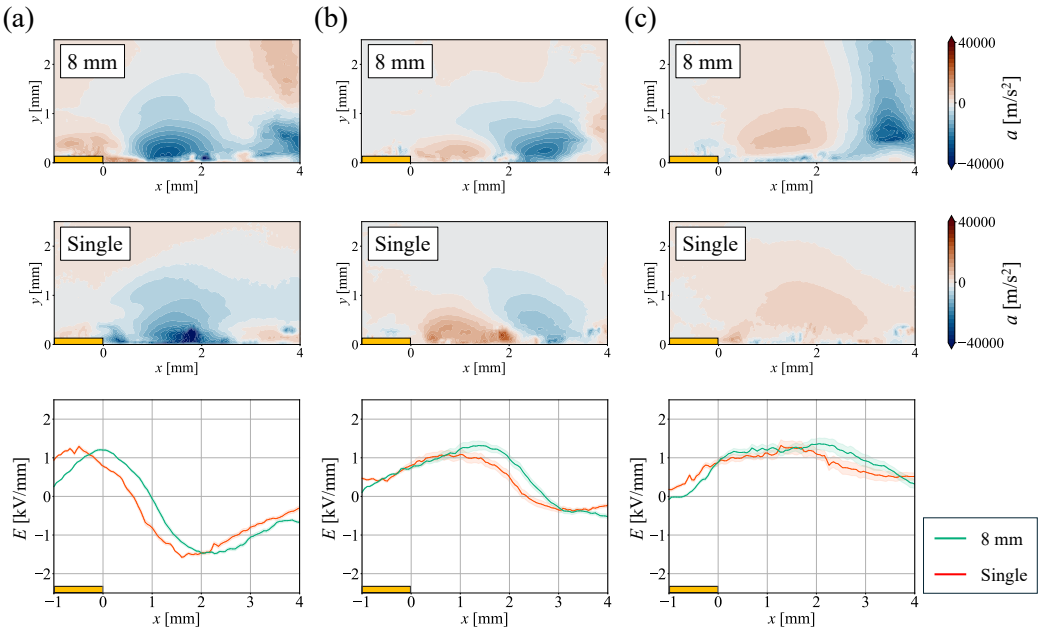


Figure 11. Comparison of x-directional acceleration term fields and surface electric field profiles during the positive-going phase ($0°, 45°, 90°$). The top and middle panels display the acceleration term distribution for the LPSJA ($\lambda = 8$ mm) and Single PA, respectively, while the bottom panel shows their corresponding electric field distributions.In the bottom panel, the solid lines represent the electric field profiles derived from the gradient of the surface potential averaged across the 66th to 99th voltage cycles, and the error envelopes represent the 95% confidence interval calculated over the 33 cycles. A key trade-off is observed: although the LPSJA consistently exhibits a stronger electric field (bottom panel), its acceleration term (top panel) becomes lower than that of the Single PA at 45° (b). This indicates that the electrical enhancement from the "memory effect" is partially counteracted by fluid dynamic losses arising from the collision of opposing ionic winds.

(Fig. 12(e)), reflecting the continuous propagation of the negative discharge front.

The resulting acceleration term fields are discussed in relation to these electrical trends. In the 180° (Fig. 12(d)), a positive acceleration region (red) emerges near the electrode edge ($x < 1$ mm) for both cases. This acceleration region corresponds to the negative electric field area, which is consistent with the mechanism of EHD force generation driven by negative ions. However, the acceleration term for the LPSJA remains smaller than that of the Single PA in this specific phase. This suggests that at the very beginning of the negative-going phase, the positive acceleration induced by the EHD force is still prevented by the residual fluidic interference. In contrast, during the 225° (Fig. 12(e)), the LPSJA exhibits a significant increase in acceleration, significantly surpassing the Single PA. This indicates that as the negative electric field enhancement by the memory effect moves further downstream, the promoted EHD force generation becomes dominant enough to overcome these fluid dynamic losses. Consequently, the electrical superiority of the LPSJA is successfully converted into a higher resulting acceleration term during this phase. Finally, by the 270° phase (Fig. 12(f)), both the electric field and acceleration term diminish as the voltage reaches its negative peak.

In summary, the interaction between opposing electrodes characterizes the EHD force response through several coupled processes. The proximity of the opposing electrode leads to an increase in surface charging due to discharge interference, and these accumulated charges persist until the onset of the subsequent discharge polarity, thereby enhancing the memory effect and local electric field. This strengthened electric field promotes the motion of charged particles and enhances the potential for EHD force generation. However, the final ionic wind strengths are ultimately determined by a trade-off between this electrical enhancement and fluid dynamic losses, such as the adverse pressure gradients inherent in the colliding jet configuration.

3.2 Influence of electrode distance on LPSJA

The influence of the electrode distance λ on the flow field is presented in Fig. 13, which shows the temporal evolution of the maximum x-directional velocity for various λ. While all conditions exhibit the same trend of deceleration and acceleration cycle, a smaller electrode distance leads to a

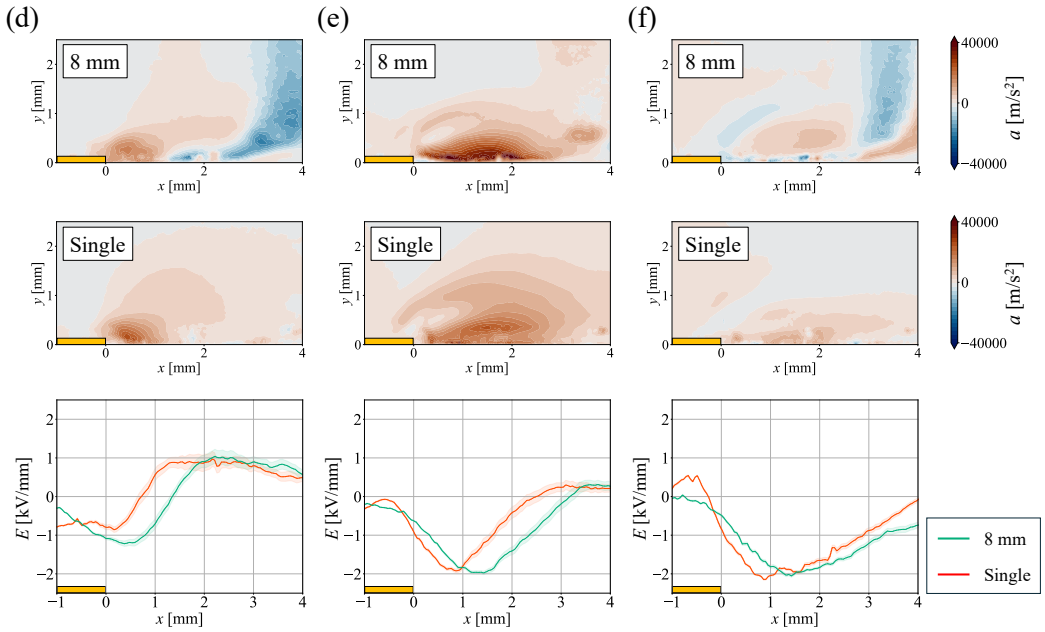


Figure 12. Comparison of x-directional acceleration term fields and surface electric field profiles during the negative-going phase $(180°, 225°, 270°)$. A dominant electrical advantage is observed: although fluidic interference initially restricts acceleration term at 180° (d), the LPSJA exhibits a significant increase in acceleration term by 225° (e), significantly surpassing the Single PA. This demonstrates that the enhanced negative electric field, driven by the surface charge memory effect, eventually overcomes fluid dynamic losses to produce a higher net EHD force.

noticeably earlier and more pronounced velocity change (before 0° and after 180°). The temporal flow velocity change suggests that the dynamic balance between the EHD force and fluid dynamic losses is significantly altered by the electrode configuration.

As demonstrated by the potential and electric field distributions (Fig. 14 and 15), reducing the electrode distance λ significantly strengthens the local electric field. This is due to the enhanced memory effect, especially during the discharge onset. However, the duration of this memory effect is found to be sensitive to the electrode distance. At the extreme proximity of $\lambda = 4$ mm, the discharge regions originating from the opposing electrodes begin to overlap significantly. This spatial overlap facilitates the immediate neutralization of accumulated surface charges by the opposing plasma, shortening the time the surface remains charged (Fig. 14 (d)-(e)). Consequently, the memory effect is prematurely weakened. This results in a shorter duration of the Electric field and the EHD force enhancement compared to cases with larger λ. In addition to these electrical constraints, the electrical promotion is also countered by fluid dynamic losses as λ decreases. At small λ, the opposing ionic winds collide with higher momentum because of the reduced interaction distance, forming an intense high-pressure region that induces a strong negative acceleration (flow deceleration). Specifically, for $\lambda = 4$ mm, this fluid dynamic penalty becomes dominant enough to outweigh the initial electrical gain, resulting in a lower maximum velocity despite the stronger peak electric field. Consequently, the velocity evolution observed in Fig. 13 are determined by a critical trade-off: while a compact configuration increases the electrical potential for EHD force generation, it simultaneously intensifies fluid dynamic resistance and restricts the temporal sustainability of the EHD force.

3.3 Macroscopic Performance and Efficiency

The local modifications in surface potential and electric field distributions directly influence the overall performance of the LPSJA. Figure 16 shows the normalized power consumption P_{elec} where the values are divided by the total effective span length of the electrodes. Generally, the results indicate that the LPSJA consumes less power than the Single PA across the measured voltage range. To characterize the voltage-power relation, the power law $P_{elec} = a(V - V_0)^n$ was employed. The discharge onset voltage V_0 and the exponent n were determined using a least-squares optimization. The analysis reveals that as the electrode distance λ decreases to 6 mm and 4 mm, V_0 significantly increases compared to the Single PA and cases with larger λ. The increase in the V_0 suggests that the proximity of the opposing electrodes suppresses discharge formation.

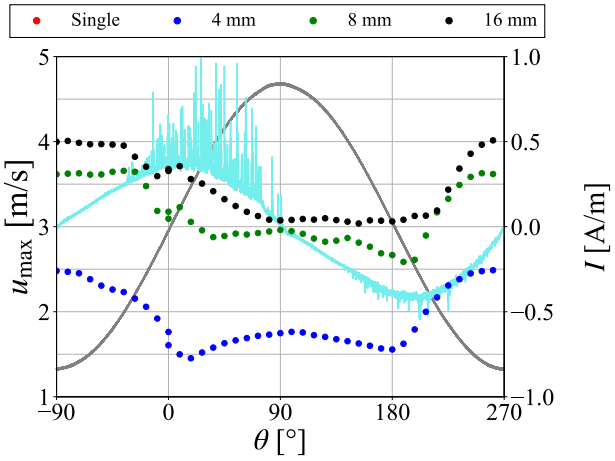


Figure 13. Effect of electrode distance λ on the temporal evolution of maximum x-directional velocity u_{max}. While the overall deceleration and acceleration cycle remains consistent across all cases, a reduction in λ leads to an earlier onset and a greater magnitude of velocity response.

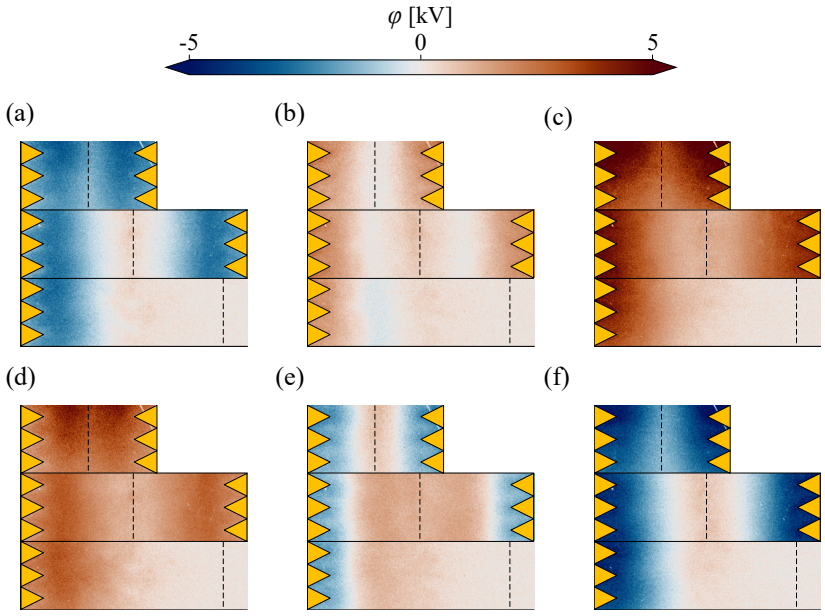


Figure 14. Influence of electrode distance λ on the spatio-temporal evolution of surface potential. Figures (a)–(c) and (d)–(f) show the positive-going and negative-going phases, respectively. Within each figure, the top, middle, and bottom sections compare $\lambda = 4$ mm, 8 mm, and 16 mm. Note the significant spatial overlap of discharge regions at $\lambda = 4$ mm, which facilitates rapid surface charge neutralization by counter-ions from the opposing plasma.

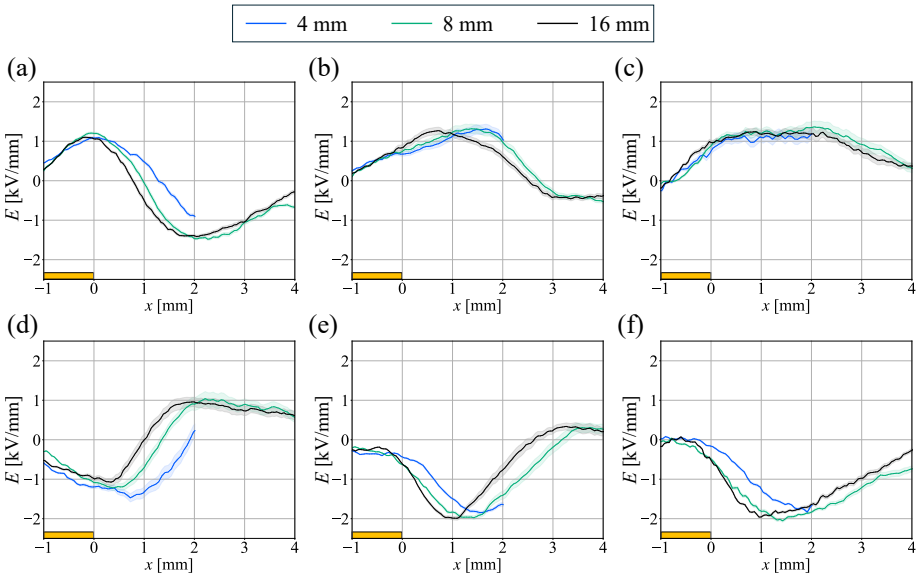


Figure 15. Comparison of x-directional electric field profiles for various electrode distances λ. Figure (a)–(c) and Fig. (d)–(f) show the positive-going phase ($0°, 45°$, and $90°$) and negative-going phases ($180°, 225°$, and $270°$), respectively. The solid lines represent the electric field profiles derived from the gradient of the surface potential averaged across the 66th to 99th voltage cycles, and the error envelopes represent the 95% confidence interval calculated over the 33 cycles.A critical trade-off between magnitude and duration is observed: while the smallest distance ($\lambda = 4$ mm) produces the highest peak electric field, this enhancement diminishes prematurely due to accelerated charge neutralization.

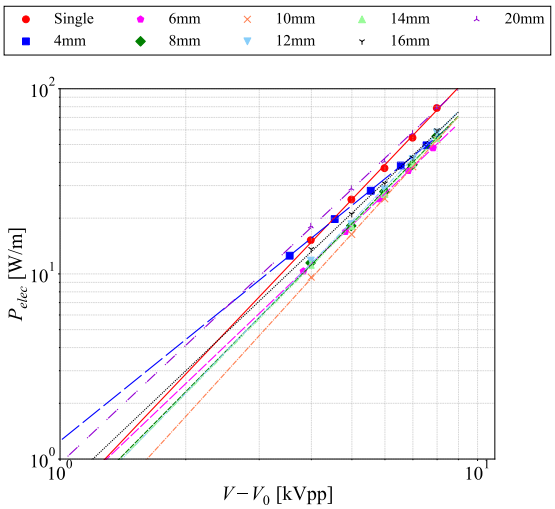
Furthermore, at the smallest distance ($\lambda = 4$ mm), the exponent n decreases to approximately 1.82, which is notably lower than the standard range for a Single PA. This dual trend suggests that mutual interference between opposing discharge regions fundamentally limits the discharge. The spatial confinement delays the onset of discharge (higher V_0) and simultaneously inhibits its expansion at higher voltages (lower n). Consequently, these electrical constraints effectively restrict the growth of power consumption in the compact LPSJA configuration.

To evaluate the fluid control capability, the upward momentum flow rate M of vertical ionic wind and the power conversion efficiency $\eta = K/P_{elec}$ were derived from the PIV velocity fields (Fig. 17). Here, K represents the upward kinetic energy flow rate of the jet. Both M and K were evaluated across the horizontal cross-section corresponding to the position of the maximum vertical velocity (v_{max}). The results reveal that both M and η are strongly dependent on the electrode distance λ, reaching their maximum values at $\lambda = 12, 16$ mm. As λ decreases below this optimal value, the momentum flow rate deteriorates despite the electrical enhancement as stated in the previous sections.

This momentum flow rate behavior is explained by the trade-off between the electrical enhancement of EHD force and fluid dynamic losses. As discussed in previous sections, a smaller λ increases surface charge accumulation and strengthens the local electric field via the memory effect, which potentially enhances EHD force generation. However, this electrical benefit is increasingly offset by two major factors: the accelerated neutralization of surface charges and the intensified adverse pressure gradient. Specifically, at very small λ, the high-velocity collision of opposing ionic winds in a confined space creates a steep pressure gradient. This pressure rise acts as a substantial fluid dynamic resistance, which prevents the further development of the flow. Consequently, optimizing the electrode distance λ is essential for LPSJA design; it requires balancing the gain in driving force from surface charge effects against the fluidic losses inherent in the colliding jet configuration.

4 Conclusion

We experimentally investigated how electrode distance (λ) affects surface charge and electric field distribution in LPSJA, and how these changes influence the ionic wind. Phase-resolved analysis clarified that a smaller λ promotes positive charge accumulation near the center, significantly enhancing the local electric field for EHD force generation. This enhancement was reflected in the acceleration term fields (Du/Dt), showing earlier and stronger flow drive at the onset of the



$P_{elec} = a(V - V_0)^n$			
λ	a	V_0	n
Single	0.556	2.014	2.37
4 mm	1.25	2.452	1.82
6 mm	0.576	2.174	2.15
8 mm	0.475	2.018	2.28
10 mm	0.304	2.005	2.48
12 mm	0.451	2.014	2.33
14 mm	0.460	2.013	2.29
16 mm	0.679	2.004	2.14
20 mm	0.945	2.014	2.12

Figure 16. Power consumption characteristics of the LPSJA. The left figure compares the normalized power consumption P_{elec} (power per unit electrode span length) across different λ values, while the right table lists the fitting parameters for the power-law equation $P_{elec} = a(V - V_0)^n$.The parameters V_0 and n were determined through least-squares optimization to maximize the R^2 coefficient. Notably, at smaller λ values (4 mm and 6 mm), an increase in V_0 and a reduction in n (down to ≈ 1.82 at $\lambda = 4$ mm) are observed. This dual trend indicates that spatial confinement and mutual interference between opposing discharge regions not only delay the discharge onset but also inhibit its expansion at higher voltages.

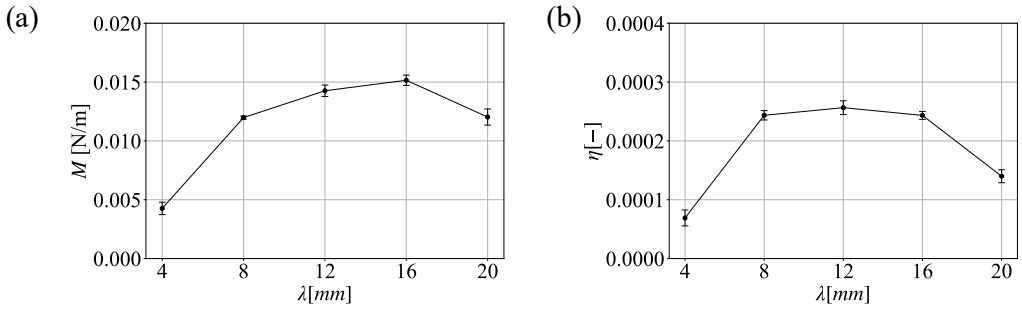


Figure 17. Fluid control capability of LPSJA as a function of electrode distance λ. (a) Upward momentum flow rate M and (b) power conversion efficiency η, both evaluated at the cross-section of maximum vertical velocity. The error bars represent the 95% confidence interval calculated from over five independent measurements. The results identify an optimal range at $\lambda = 12$, 16 mm, where the LPSJA achieves its peak performance. This peak represents the physical limit where the electrical enhancement from the surface-charge memory effect is most effectively utilized before being overwhelmed by fluid dynamic losses and accelerated charge neutralization at smaller λ.

discharge phase. However, the sustainability of this electrical benefit is limited by the proximity of the electrodes. At the extreme proximity of $\lambda = 4$ mm, the spatial overlap of opposing discharges leads to the rapid neutralization of surface charges, prematurely weakening the electric field enhancement. Furthermore, the acceleration reveals a critical trade-off: while the EHD force is locally promoted, the collision of opposing ionic winds induces a steep adverse pressure gradient. This fluid dynamic penalty, along with the inhibited discharge development — evidenced by an increased discharge onset voltage (V_0) and a reduced power-law exponent (n) — restricts the overall flow velocity and momentum flow rate at smaller λ. In summary, the performance of the LPSJA is governed by the competition between EHD force promotion via the memory effect and fluid dynamic losses inherent in the colliding jet configuration. Therefore, optimizing λ is essential to effectively convert the electrical potential of the enhanced field into resulting flow acceleration. These findings provide a physical foundation for determining the optimal configuration and driving conditions of LPSJAs for effective flow control. Future work will investigate electric field characteristics considering spatial dimensions, examine EHD effects under varying driving conditions, and explore further integration of LPSJA. Ultimately, we aim to propose optimal installation and driving conditions for LPSJA based on the desired EHD effect.

Acknowledgments
We are grateful to Y Kaneko and T Uemura for their helpful experimental support.

Funding
This work was supported by JSPS KAKENHI Grant Numbers 25K01419.

Author contributions
Yuki Ishii: Writing – Original Draft, Software, Methodology, Investigation, Visualization, Formal analysis. **Atsushi Komuro**: Writing - Review & Editing, Conceptualization, Methodology, Resources. **Shūji Ōtomo**: Writing - Review & Editing, Formal analysis, Supervision. **Hiroyuki Nishida**: Writing - Review & Editing, Conceptualization, Methodology, Supervision.

References

[1] Nicolas Benard and Eric Moreau. Electrical and mechanical characteristics of surface ac dielectric barrier discharge plasma actuators applied to airflow control. *Experiments in Fluids*, 55(11):1846, 2014.

[2] Hiroyuki Nishida. Contributions of plasma simulations to physical understanding of surface dielectric barrier discharge for flow control (invited paper). *J. Electrostat.*, (104115):104115, June 2025.

[3] Thomas C. Corke, C. Lon Enloe, and Stephen P. Wilkinson. Dielectric barrier discharge plasma actuators for flow control*. *Annual Review of Fluid Mechanics*, 42(Volume 42, 2010):505–529, 2010.

[4] Eric Moreau. Airflow control by non-thermal plasma actuators. *Journal of Physics D: Applied Physics*, 40(3):605, jan 2007.

[5] Satoshi Shimomura, Satoshi Sekimoto, Akira Oyama, Kozo Fujii, and Hiroyuki Nishida. Closed-loop flow separation control using the deep q network over airfoil. *AIAA Journal*, 58(10):4260–4270, 2020.

[6] Thomas C. Corke and Flint O. Thomas. Active and passive turbulent boundary-layer drag reduction. *AIAA Journal*, 56(10):3835–3847, 2018.

[7] Richard D Whalley and Kwing-So Choi. Turbulent boundary-layer control with plasma spanwise travelling waves. *Exp. Fluids*, 55(8), August 2014.

[8] Kwing-So Choi, Timothy Jukes, and Richard Whalley. Turbulent boundary-layer control with plasma actuators. *Philos. Trans. A Math. Phys. Eng. Sci.*, 369(1940):1443–1458, April 2011.

[9] Flint O. Thomas, A. Kozlov, and Thomas C. Corke. Plasma actuators for cylinder flow control and noise reduction. *AIAA Journal*, 46(8):1921–1931, 2008.

[10] Timothy N. Jukes and Kwing-So Choi. Flow control around a circular cylinder using pulsed dielectric barrier discharge surface plasma. *Physics of Fluids*, 21(8):084103, 08 2009.

[11] Yutaka Kaneko, Shūji Ōtomo, Taisuke Torin, Yusuke Kakuya, Takafumi Saito, Tatsuhiko Hanai, Takashi Matsuno, and Hiroyuki Nishida. The combination of rear flaps and plasma actuators for the drag reduction of a square-back bluff body. *Journal of Fluids Engineering*, 147(12):121201, 06 2025.

[12] Frederico Rodrigues, Mohammadmahdi Abdollahzadehsangroudi, João Nunes-Pereira, and José Páscoa. Recent developments on dielectric barrier discharge (DBD) plasma actuators for icing mitigation. *Actuators*, 12(1):5, December 2022.

[13] Nima Amanifard, Hesam Moayedi, Farid Dolati, and Hamed Mohaddes Deylami. A review of recent advancements in electrohydrodynamic heat transfer enhancement. *J. Electrostat.*, 137(104151):104151, September 2025.

[14] Yang Liu, Cem Kolbakir, Haiyang Hu, and Hui Hu. A comparison study on the thermal effects in DBD plasma actuation and electrical heating for aircraft icing mitigation. *Int. J. Heat Mass Transf.*, 124:319–330, September 2018.

[15] Naoki Omori, Akinori Nishizawa, Asami Hatamoto, Shūji Ōtomo, and Hiroyuki Nishida. Experimental evaluation of gas heating and flow modification effects by plasma actuator in forced-convection heat transfer. *International Journal of Heat and Mass Transfer*, 247:127136, 2025.

[16] Arvind Santhanakrishnan, Jamey Jacob, and Yildirim Suzen. Flow control using plasma actuators and linear/annular plasma synthetic jet actuators. In *3rd AIAA Flow Control Conference*, Reston, Virigina, June 2006. American Institute of Aeronautics and Astronautics.

[17] Jin-Jun Wang, Kwing-So Choi, Li-Hao Feng, Timothy N Jukes, and Richard D Whalley. Recent developments in DBD plasma flow control. *Prog. Aerosp. Sci.*, 62(C):52–78, October 2013.

[18] Marc T Hehner, Davide Gatti, and Jochen Kriegseis. Stokes-layer formation under absence of moving parts—a novel oscillatory plasma actuator design for turbulent drag reduction. *Phys. Fluids (1994)*, 31(5):051701, May 2019.

[19] Karthikeyan Kv and Harish. Advancements in flow control using plasma actuators: A comprehensive review. *Eng. Res. Express*, 7(1):0–0, January 2025.

[20] Timothy N Jukes and Kwing-So Choi. Dielectric-barrier-discharge vortex generators: characterisation and optimisation for flow separation control. *Exp. Fluids*, 52(2):329–345, February 2012.

[21] Zongnan Chen and Chih-Yung Wen. Flow control of a D-shaped bluff body using different DBD plasma actuators. *J. Fluids Struct.*, 103(103292):103292, May 2021.

[22] Julie A Vernet, Ramis Örlü, David Söderblom, Per Elofsson, and P Henrik Alfredsson. Plasma streamwise vortex generators for flow separation control on trucks: A proof-of-concept experiment: A proof-of-concept experiment. *Appl. Sci. Res.*, 100(4):1101–1109, February 2018.

[23] Michael Wicks, Flint O. Thomas, Thomas C. Corke, Mehul Patel, and Alan B. Cain. Mechanism of vorticity generation in plasma streamwise vortex generators. *AIAA Journal*, 53(11):3404–3413, 2015.

[24] Takafumi Saito, Hiroyuki Nishida, Yutaka Kaneko, and Yusuke Kakuya. Effect of interference between two facing plasma actuators on discharge and flow field. In *AIAA SCITECH 2023 Forum*, page 0863, 2023.

[25] R A Humble, S A Craig, J Vadyak, P D McClure, J W Hofferth, and W S Saric. Spatiotemporal structure of a millimetric annular dielectric barrier discharge plasma actuator. *Phys. Fluids (1994)*, 25(1):017103, January 2013.

[26] Tom Fridlender, Srikar Yadala Venkata, Nicolas Benard, and Eric Moreau. Electrical characteristics and flow topology of ring-type dielectric barrier discharge plasma actuator. In *AIAA SCITECH 2023 Forum*, Reston, Virginia, January 2023. American Institute of Aeronautics and Astronautics.

[27] Huw Borradaile, Konstantinos Kourtzanidis, Francois Rogier, Kwing-So Choi, and Xuerui Mao. Flow reversal in millimetric annular dbd plasma actuator. *Journal of Physics D: Applied Physics*, 54(34):345202, 2021.

[28] Y Lagmich, Th Callegari, L C Pitchford, and J P Boeuf. Model description of surface dielectric barrier discharges for flow control. *J. Phys. D Appl. Phys.*, 41(9):095205, May 2008.

[29] Ronny Brandenburg. Dielectric barrier discharges: progress on plasma sources and on the understanding of regimes and single filaments. *Plasma Sources Sci. Technol.*, 26(5):053001, March 2017.

[30] Shintaro Sato and Naofumi Ohnishi. Role of surface discharge dynamics in the generation of electrohydrodynamic force: toward performance improvement of dielectric barrier discharge plasma actuators. *J. Phys. D Appl. Phys.*, 58(14):143002, April 2025.

[31] Shintaro Sato, Kodai Mitsuhashi, Tomoki Enokido, Atsushi Komuro, Akira Ando, and Naofumi Ohnishi. Surface-charge control strategy for enhanced electrohydrodynamic force in dielectric barrier discharge plasma actuators. *J. Phys. D Appl. Phys.*, 54(45):455203, November 2021.

[32] Akiko Kumada, Yasuhiro Shimizu, Masakuni Chiba, and Kunihiko Hidaka. Pockels surface potential probe and surface charge density measurement. *Journal of electrostatics*, 58(1-2):45–58, 2003.

[33] Takuma Uemura, Hiroyuki Nishida, Ryo Ono, and Atsushi Komuro. Effect of nitrogen/oxygen ratios on surface charge distributions generated by repetitive surface dielectric barrier discharges. *Plasma Sources Science and Technology*, 33(6):065011, jun 2024.

[34] M L Jakobsen, T P Dewhirst, and C A Greated. Particle image velocimetry for predictions of acceleration fields and force within fluid flows. *Meas. Sci. Technol.*, 8(12):1502–1516, December 1997.

[35] China Natsume, Atsushi Komuro, and Akira Ando. Characterisation of surface charge density and net electric field during parallel-plate dielectric barrier discharge generated in atmospheric-pressure air. *Plasma Sources Sci. Technol.*, 31(9):095019, September 2022.

[36] J P Boeuf, Y Lagmich, and L C Pitchford. Contribution of positive and negative ions to the electrohydrodynamic force in a dielectric barrier discharge plasma actuator operating in air. *J. Appl. Phys.*, 106(2):023115, July 2009.